

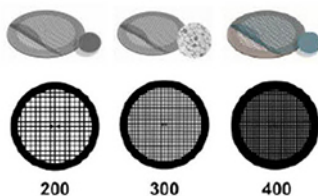
Nanocharacterization by TEM and AFM

We offer a wide range of TEM and AFM tools, from TEM grids and finders to AFM substrates and grippers.

Available in a wide variety of designs and materials to support your work, select from a broad range of mesh sizes, specimen supporting films, and materials that perfectly suit the conditions of your TEM analysis.

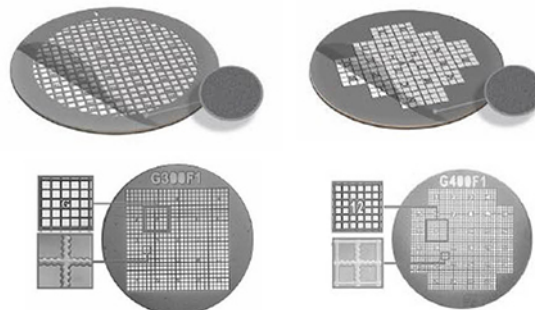
TEM grid specifications:

Material	Mesh Size and Shape	Film Specifications
• Cu	• Square or hexagonal	• None
• Ni	• Single-hole grid (75 mm or 100 mm)	• Continuous formvar film (thicknesses: 5-6 nm, 10 nm)
• Au	• 100	• Lacey carbon film (average hole sizes: 50 nm, 100 nm, 150 nm, 100 nm, 150 nm)
• Mo	• 150	• Continuous amorphous carbon film (thicknesses: 10 nm, 20-30 nm)
• Cu/Pd	• 200	• Continuous formvar/carbon film (thickness: 10nm formvar and 1nm carbon)
	• 300	
	• 400	



TEM finder grid specifications:

Material	Mesh Size	Film Specifications
• Cu	• 135	• None
• Ni	• 200	• Continuous amorphous carbon film (thicknesses: 3-4 nm, 10 nm, 20-30 nm)
• Au	• 300	
	• 400	



Supporting Tools for Nanomaterial Characterization

Our comprehensive range of supporting materials for nanomaterial characterization includes tweezers (sharp tip, disc gripper for AFM), TEM window grids (various thicknesses, 1 or 9 windows), a magnetic pick-up tool, a grid storage box, cryo-capsules, lift-out grids (Cu or Mo), AFM substrates (various dimensions), and much more.



Explore our complete range of TEM grids on: SigmaAldrich.com/nanocharacterization

© 2022 Merck KGaA, Darmstadt, Germany and/or its affiliates. All Rights Reserved. Merck, the vibrant M, and Sigma-Aldrich are trademarks of Merck KGaA, Darmstadt, Germany or its affiliates. All other trademarks are the property of their respective owners. Detailed information on trademarks is available via publicly accessible resources.

MK_AD9792EN 43729 08/2022

The Life Science business of Merck operates as MilliporeSigma in the U.S. and Canada.

Sigma-Aldrich®
Lab & Production Materials

Modeling of Carbon Black Fragmentation During High-Intensity Dry Mixing Using the Population Balance Equation and the Discrete Element Method

Ernek Asylbekov,* Julian Mayer, Hermann Nirschl, and Arno Kwade

A complex interaction between the process design and the properties of carbon black (CB) during dry mixing of cathode material influences the microstructure and thus the performance of the Li-ion battery. The description of these interactions by means of a coupling of the mixing process simulation and the fragmentation of CB is the focus of this work. The discrete element method provides information about the frequency and intensity of the stress. The change of the CB size distribution is done by the population balance equation. The material strength as well as the fracture behavior are represented with simple models. The calibration of the model parameters is performed using the Nelder–Mead algorithm. The calibrated models provide good agreement with the measurements of the size distributions from experimental investigations. Transfer of the calibrated parameters to other process settings is possible and provides good agreement in some cases. Recalibration of the fracture behavior improves the accuracy of the model so that it can be used as a predictive tool.

1. Introduction

One of the biggest challenges in the transition from fossil fuels to renewable energies is the development of suitable energy storage systems. Over the past decade, Li-ion batteries have proven to be a reliable solution for many applications. Since their introduction in the 1990s, their sales have increased thanks to the expansion of the electronics market. In the past decade, the use of Li-ion batteries in electric vehicles has led to a rapid increase in demand for high-capacity batteries.^[1] These developments put the Li-ion

battery in the focus of the international research community. Since then, the goal has been to improve battery performance, capacity, and lifetime. Previous work showed that, in addition to the materials chosen, the microstructure of the electrodes is critical to cell performance.^[2–4] Further research revealed the complex relationship between the cell manufacturing process, which determines the electrode particle structure, and the functionality of the finished batteries.^[5–7] These findings required deeper insight into the component interactions, particularly in the early stages of production, that determine structure formation.

An important element of the composite, especially in the cathodes, are the conductive additives such as carbon black (CB).


They compensate for the overall poor conductivity of the active material and have a significant impact on the structural properties.^[8,9] In addition, a proper distribution of CB in the electrode layer is critical to battery performance.^[10] However, the microstructure of the CB changes due to the shear stresses that occur during the fabrication process, and therefore also affects the overall capacity and performance of the battery.^[11] Therefore, much of the current research is focused on studying the relationship between the manufacturing process and the final electrode structure.^[12,13] For these reasons, the present work will focus mainly on the cathode. It is worth noting that the term cathodes here refer to the discharge process. The authors retain this terminology throughout the article.

Since extensive experimental parameter studies are time and material consuming, simulative studies of the dispersion process are a promising alternative. These do not require the use of expensive materials or sophisticated analytical methods, but provide a detailed insight into what happens during the manufacturing process. For this reason, the objective of this article is to simulative investigate the fracture of CB aggregates during the dry dispersion process of the cathode material in intensive mixers. However, the reliability of the simulation results is highly dependent on the models used. Finding a suitable approach with sufficient accuracy while keeping the computational cost reasonable is a major challenge for simulative studies.

Modeling the change in the particle size distribution of CB is the main focus of this work. The aim is to represent the particle size change during the comminution process of CB during dry

E. Asylbekov, H. Nirschl
Institute of Mechanical Process Engineering and Mechanics
Karlsruher Institut für Technologie
76131 Karlsruhe, Germany
E-mail: ermek.asylbekov@kit.edu

J. Mayer, A. Kwade
Institute for Particle Technology
Technische Universität Braunschweig
38106 Braunschweig, Germany

 The ORCID identification number(s) for the author(s) of this article can be found under <https://doi.org/10.1002/ente.202200867>.

© 2022 The Authors. Energy Technology published by Wiley-VCH GmbH. This is an open access article under the terms of the Creative Commons Attribution-NonCommercial License, which permits use, distribution and reproduction in any medium, provided the original work is properly cited and is not used for commercial purposes.

DOI: 10.1002/ente.202200867

processing as accurately as possible. At the same time, it is intended to better understand the mechanisms during comminution by finding suitable models. Similar challenges were tackled in the past by numerous publications. Most describe the change of particle size by means of the population balance approach. This method offers a very intuitive description of the change of arbitrary particle properties, which are quantified by a set of suitable variables. The entire particle population can then be described by means of the density (usually number, volume, or mass density) of these properties. With respect to conservation laws, transport equations describe the behavior of the particles within the property space.^[14] This flexibility allowed numerous applications in crystallization, granulation, mixing, and grinding.^[15–21] Such formulations require a description of dominant mechanisms, which are often referred to as kernels. The influences of the environment are captured in these terms. In the field of comminution, the modeling of grinding processes in ball mills is particularly common. Here, the influence is described as the energy which is introduced into the grinding. Early publications reduce this quantity to the applied specific energy of the mill^[22,23] or the mean impact energy, which balls apply to the material.^[24–27] Others emphasize that such single parameters are not sufficient and that a distribution of impact energies is necessary for better accuracy.^[28] Simulations of the particle collisions within the mills using discrete element methods (DEMs) provide information on the spatial and temporal distribution of the impact energies.^[24–26,29,30] This literature provides a well-elaborated and reliable approach to the study of the problem at hand. However, on closer inspection, the presented methods are not suitable for precise modeling of CB fragmentation. Since in the used device the occurring fracture is dominated less by impact energies and more by compression and shear, previous methods don't capture this process. Furthermore, in contrast to the existing literature, the assumption that every impact leads to fracture does not apply here. Also, in the present case, the fragmentation of a bulk with a broad size distribution must be considered completely resolved. This requires a particle size-dependent breakage rate. In contrast, the presented literature mostly considers a homogeneous breakage rate or only regards mass reduction of the initial size class.

The material-specific properties of the CB as well as the process properties have to be defined and modeled. On the one hand, a well set up model can provide a predictive tool for the design and control of the manufacturing process. On the other hand, it can provide insight into the complex interactions of dry dispersion of CB. Furthermore, it supports the development of energy-efficient manufacturing of cells with low-cost process optimization and predictive control.

2. Methodology

Figure 1 shows the schematic structure of the presented study. The population balance equation is the heart of the presented work. Its key terms are the breakage rate and the breakage function. The individual aspects of modeling will now be discussed in more detail.

2.1. Linear Breakage Equation

The linear breakage equation is a version of the population balance approach. Here, the entire mixer is regarded as one domain and the spatial distribution of the particles is neglected. Thus, we obtain the classic linear breakage equation as already described by Ramkrishna.^[14] It describes the time variation of the number density distribution $f(x, t)$ for particles with volume x at time t . By inserting an initial condition $f(x, 0)$ it can be integrated up to time t to retrieve $f(x, t)$.

$$\frac{\partial f(x, t)}{\partial t} = \int_x^\infty p(x, \gamma) b(\gamma) f(\gamma, t) d\gamma - b(x) f(x, t) \quad (1)$$

The right-hand side of the integrodifferential equation consists of two terms, which are usually referred to as birth and death functions. The birth function describes the increase in the number of smaller particles due to the breakage of larger particles. The function $b(\gamma)$ describes the breakage rate of particles with volume γ and $p(x, \gamma)$ describes the breakage function. The death function describes the loss of particles with volume x due to breakage with a breakage rate of $b(x)$.

2.2. Numerical Integration

As shown earlier, the population balance approach results in a partial differential equation, the right-hand side of which is presented later. The left-hand side of the balance is the partial time derivative of the number-based density distribution of particles $f(x, t)$. For simple formulations of the birth and death terms, analytical solutions for $f(x, t)$ exist in the literature.^[31] For complex formulations, different approaches exist. These often exploit the linearity and self-similarity of the equation and are summarized in numerous publications.^[14,32] In this work, the goal is to represent the entire resolved particle size distribution. For this reason, methods of moments such as the quadrature method of moments (QMOM) are less suitable. The method of classes (MOCs) offers the possibility of a fully resolved view of distributions. In this method, the particle size distribution is divided into size classes similar to a sieve analysis. This method is very intuitive and the numerical implementation is very simple. First, the particle size range has to be set to $(0, x_{\max}]$ and divided into N cells. Here, cell i contains particles in the size range $(x_{i-1/2}, x_{i+1/2}]$ with $i = 1 \dots N$. The edges of the considered domain are at $x_{1/2} = 0$ and $x_{N+1/2} = x_{\max}$. The value f_i represents the mean value of the distribution $f(x, t)$ within the size class i at the point $x_i = (x_{i+1/2} + x_{i-1/2})/2$. For particle distributions with a wide range, a logarithmic scale for x_i is recommended which is why it is used in this work.

$$f_i \approx \frac{1}{\Delta x} \int_{x_{i-1/2}}^{x_{i+1/2}} f(x, t) dt \quad (2)$$

$$\text{with } \Delta x = x_{i+1/2} - x_{i-1/2} \quad (2a)$$

However, the quality of the results depends significantly on the number of individual classes. This results in higher

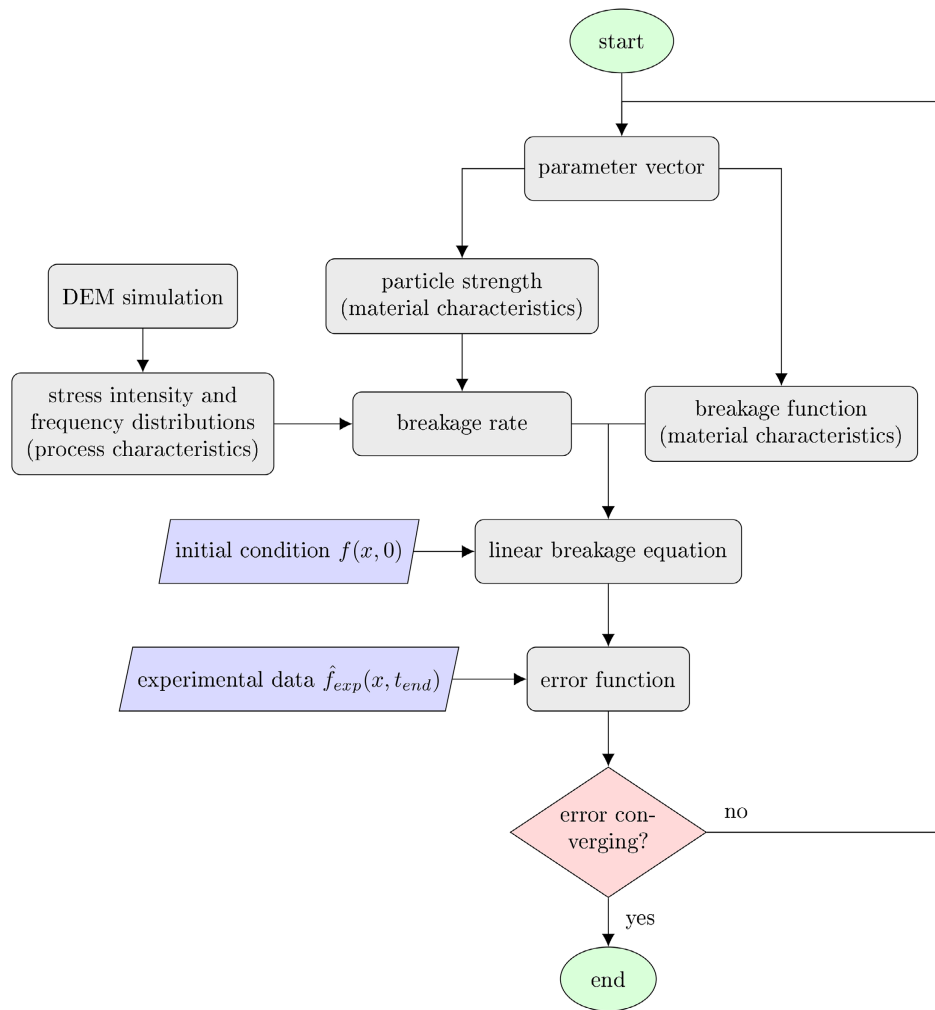


Figure 1. A schematic structure of the presented workflow.

computation times compared to methods of moments. A greater challenge is the implementation of the mandatory conservation of mass. Due to the discretization in size classes, very fine grids are necessary. Kumar et al. presented a correction term that ensures mass conservation independent of the lattice resolution^[33]

$$\frac{d\hat{f}_i}{dt} = \frac{1}{\Delta x_i} \sum_{k=i}^N \omega_k^b b_k P_{ik} \hat{f}_k \Delta x_k - \omega_i^d b_i \hat{f}_i, \quad i = 1, \dots, N \quad (3)$$

where

$$P_{ik} = \int_{x_{i-1/2}}^{x_i} p(x, x_k) dx \quad (4a)$$

$$\omega_k^b = \frac{x_k(\nu(x_k) - 1)}{\sum_{i=1}^{k-1} (x_k - x_i) P_{ik}} \quad \text{and} \quad \omega_k^d = \frac{\omega_k^b}{x_k} \sum_{i=1}^k x_i P_{ik}, \quad (4b)$$

$k = 2, \dots, N$

$$\hat{x}_k^i = \begin{cases} x_i & \text{when } k = i \\ x_{i+1/2} & \text{otherwise.} \end{cases} \quad (4c)$$

Equation (3)a–c shows the population balance discretized using the MOC with the corrections of Kumar et al. Here ω^b and ω^d are the weights for the birth and death terms.

The time integration of the differential equation is performed using a classical Runge–Kutta method. The four-step method, often denoted RK4, approximates the derivative by averaging the slope at four points. Thus, time steps with $\Delta t \leq 0.1$ s result in almost time-step independent results.

2.3. Birth and Death Terms

2.3.1. Breakage Function

The right-hand side of the population balance equation contains information on material and process characteristics. The breakage function $p(x, \gamma)$ is the distribution of fragments with volume x resulting from the breakage of a particle with volume γ . To

satisfy the boundary condition of mass conservation, the following conditions must be fulfilled

$$\int_0^{\gamma} p(x, \gamma) dx = \nu(\gamma) \quad (5a)$$

$$p(x, \gamma) = 0 \quad \forall x \geq \gamma \quad (5b)$$

Furthermore, the number of fragments $\nu(\gamma)$ for a breakage event of the particle with volume γ is given by

$$\int_0^{\gamma} xp(x, \gamma) dx = \gamma \quad (6)$$

Another condition is that at least two fragments must be produced in a breakage event. The breakage function can also be simplified by a homogeneous approach to

$$p(x, \gamma) = \frac{1}{\gamma} \theta(z) \quad \text{with } z = \frac{x}{\gamma} \quad (7)$$

Here the function $\theta(z)$ represents a homogeneous breakage function with relative fragment volume z .^[32] There are countless formulations for the breakage function in the literature.^[15,34–38] The publications by Diemer and Olson^[39] and Kostoglou^[32] provide a good overview. These can be applied to different cases depending on the considered fracture behavior and the number of fragments. Hill and Ng developed generalized approaches, which they divided into product and summation functions.^[36] Diemer and Olson further simplified this approach. They reduced the parameters to the number of fragments ν and a parameter q which describes the breakage type. Theoretically, it is possible to represent every breakage function as a linear combination of the product and summation functions. The product function has a simpler and more general form

$$\theta(x) = \nu \frac{z^{q-1} (1-z)^{q(\nu-1)-1}}{B(q, q(\nu-1))} \quad \text{with } z = \frac{x}{\gamma} \quad (8)$$

For this reason, it is preferred in the present work. For $q \rightarrow 0$, the function reproduces erosion, with $q = 1$ the function represents a random fragment volume distribution. As the parameter q increases, the distribution becomes narrower until at $q \rightarrow \infty$ it corresponds to fracture into fragments of equal size. $B(x, y)$ is the Euler beta function.

2.3.2. Breakage Rate

While the literature offers numerous models for shaping the breakage function, the shape of the fracture rate is primarily dependent on the type of loading and the fracture strength of the particles. Thus, the fracture rate can be considered as a product of the contact frequency \dot{n} and the fracture probability p_s

$$b(x) = \dot{n} p_s \quad (9)$$

This approach is by no means new and has been used for modeling applications.^[40] While the contact frequency can be

obtained from DEM simulations, modeling the fracture probability requires knowledge of the distribution of stress intensity as well as information on the fracture strength of the particles.

Numerous methods exist for determining it, most of which distinguish between different types of loading (compression, impact, shear, elongation). For each type of stress, there are further subcategories, which, for example, in the case of pressure distinguish between single impact, double impact, and slow compression, to name a few. In addition to the type of stress, particle size, shape (convex or concave, round or angular, symmetrical or asymmetrical) and composition (crystalline or amorphous) are also decisive factors that not only have an enormous influence on the amount of required fracture energy, but also on the scatter of determined values. The required fracture energy is often normalized by the mass of the particle, or the applied fracture force is normalized by the particle size to a specific fracture stress.^[41] The experimental measurement of the fracture strength is a very laborious process, in which individual particles are first isolated and stressed under conditions that are to be as constant as possible. Finally, the size distribution of the fragments is analyzed.

Fortunately, the experimental measurements of fracture strength described earlier result in simple models that describe the relationship between specific energy input or fracture stress and particle size for individual bulk materials. Mostly classical power-law approaches are used, which represent a linear relationship in a double logarithmic representation.^[42] This is related, on the one hand, to the established measurement methods for characterizing particle strength on one hand and, on the other hand, to the modeling of comminution as applied mainly to ball mills. In the presented work, due to the device used, the fracture is dominated less by impact energies and more by compression and shear. Therefore, the consideration of induced stresses is more appropriate at this point. We apply a simple power-law approach of the form

$$\sigma_{\text{crit}}(x) = \sigma_0 \left(\frac{1}{x} \right)^{\frac{1}{m}} \quad (10)$$

Here $\sigma_{\text{crit}}(x)$ represents the critical breakage stress for a particle of size x , x_0 is a characteristic length and m is an exponent which sets the slope of the linear function in a double logarithmic plot.

For particularly small particles, plastic deformation becomes predominant as stated by Tavares.^[41] A particle size x_p can be defined at which the applied energy is completely transferred into plastic and elastic deformation and breakage no longer occurs. Furthermore, the specific breakage energy converges to a quasi-constant value with increasing particle size. This can be transferred from specific breakage energy to breakage stress, whereby the model takes the following form

$$\sigma_{50} = \sigma_{\infty} \left(1 + \frac{x_0}{x - x_p} \right)^{\phi} \quad (11)$$

Since particle breakage is partly influenced by stochastic effects σ_{50} is the specific fracture stress that leads to fracture with a 50% probability. σ_{∞} is the fracture stress for coarse particle sizes and x_p is the particle size at which plastic deformation

dominates the process. The characteristic length κ_0 describes the microstructure of the material and the exponent ϕ governs the curvature of the function. In this work, both models are applied and compared. The parameters result from the calibration of the resulting population balance equation. The applicability of both models is discussed in later sections.

2.4. DEM

DEM was introduced by Cundall in 1971 and has been continuously improved and applied to various particle-based problems since then.^[43] The DEM first treats a particle as a perfectly spherical element with a mass m , a radius r , and a moment of inertia I . Its translational and rotational accelerations $d\vec{u}/dt$ and $d\vec{\omega}/dt$ are given by Newton's equations as the sum of all forces \vec{F}_j and moments \vec{T}_j acting on the particle's center of gravity. The translational and angular velocities are obtained by integration over a short time step Δt .

$$\frac{m d\vec{u}}{dt} = \sum_j \vec{F}_j \quad (12a)$$

$$\frac{I d\vec{\omega}}{dt} = \sum_j \vec{T}_j \quad (12b)$$

The dominant forces in DEM include contact forces \vec{F}_c and adhesion forces \vec{F}_h . The contact forces arise from the physical interaction of two particles and are based on the elastic contact model introduced by Hertz and later extended by Mindlin and Deresiewicz.^[44,45] This approach describes the contact force as a combination of normal and tangential forces \vec{F}_c^n and \vec{F}_c^t , respectively. The basic model consists of a parallel interaction of an elastic spring with an elastic constant k and a damping element with a viscoelastic damping constant γ , both in normal and tangential directions. The normal and tangential overlaps δ^n and δ^t as well as the normal and tangential relative velocities \vec{u}_{rel}^n and \vec{u}_{rel}^t are also included in the calculation.

In this work, adhesion was modeled using the Johnson–Kendall–Roberts (JKR) model.^[46] It adds another normal force to the contact forces. This model implements the surface energy Γ into the force calculation.

A particular challenge of DEM is the high computational costs for large numbers of particles and small computational time steps as particle size decreases. In particular, for large applications with especially small particles in the nano- and micrometer ranges, simulations require not only powerful computers, but also skillful use of simplifications and assumptions. A major advantage is provided by the computation on powerful graphics cards, which have been implemented for several years. These offer the possibility to distribute the many calculations of individual particle contacts to many graphics processing units (GPUs) and thus parallelizing the very numerous calculations. The results presented in this paper were performed with the software ROCKY DEM from the developer ESSS. In combination with the powerful graphics cards of the Nvidia Tesla V100 model of the bwUniCluster of the Karlsruhe Institute of Technology (KIT), the stable simulation of large particle numbers is possible

even for very small particles. Nonetheless, simplifying assumptions are necessary to keep the computation times within a comfortable range.

In this work, DEM is used to describe the stress on the conductive additive during the dry mixing process. The influence of the process settings, in this case tip speed v_{tip} is of particular interest. The main goal is to derive relevant parameters for the calculation of the population balance equation. These include, on the one hand, the stress frequency, which indicates how often particles are stressed at certain stress. On the other hand, the stress intensity determines the probability of breakage.

The bulk is a mixture of active material and conductive additive. The active material, in this case, is NCM 622 with an average particle size of $x_{50} = 9.5 \mu\text{m}$. These particles are relatively round, and very hard with a Young's modulus of $\approx 230 \text{ GPa}$ and have a very high material density of $\rho = 4500 \text{ kg m}^{-3}$, which is not atypical for metal alloys. The conductive additive in this case is CB Super C65. The nature of CB is very complex and similar to that of silica. The basic elements of CB are primary particles with a size of $\approx 50\text{--}100 \text{ nm}$, which are formed and grow by nucleation during synthesis. These interconnect by sintered bridges to form fractal structures. Following the nomenclature introduced by Nichols et al., we refer to these as brittle agglomerates.^[47] The size and shape of brittle agglomerates vary widely, so their sizes can reach between 300 nm and more than 1 μm depending on the history and handling of the powder.^[48] The fractal dimension varies between 2.0 and 2.5 whereby the values vary greatly depending on the examined CB type. Furthermore, brittle agglomerates agglomerate into larger flakes (soft agglomerates) reaching up to 30 μm and forming even larger clumps of several millimeters during handling, storage, and transport. Due to their fractal nature, brittle agglomerates not only agglomerate by means of interparticle interactions such as Van der Waals interactions, but can also bind sterically by hooking with small side branches. This fractal structure of CB and the associated complex dispersion behavior of such nanoscale particle clusters are discussed in various publications^[7,49–52]

Due to the small size of the CB, it is not possible to completely resolve the particles in the DEM, even with low mass fractions. Even the much larger active material particles pose a challenge for a simulation of an entire mixer with only 300 g of material. Since in this case, a statistical approach to stress is of interest, an exact resolution of all particles can be omitted. For the present case, we assume the comminution of CB in this dry mixing process to be dominated by compression and shear. The much larger and tougher active material particles are compressed at the blades and the inner wall of the mixer and serve as a grinding media for the CB agglomerates which are caught in between. The CB is thereby crushed by the compression and shear in the mixer. Therefore, only the active material particles are represented in the simulation. Furthermore, it is necessary to apply the coarse-graining method. In this process, the particles are represented as larger spheres. Thus a particle in DEM represents a cluster of particles moving in the same direction with a similar velocity. This method reduces the number of particles enormously, thereby reducing the computational effort, and has since become a common method for simplifying similar tasks. For this reason, coarse-graining is also used here. The scaling laws are

derived in the literature by means of dimensional analysis.^[53,54] Furthermore, due to self-similarity the frictional force models within ROCKY do not need to be modified to satisfy the constraints from^[53,54] when Hertzian Spring Dashpot and Mindlin–Deresiewicz models are used to calculate the normal and tangential contact forces. Finally, the coefficients of friction μ_{static} , μ_{dynamic} , the coefficient of restitution e and the surface energy Γ_{SJKR} were calibrated directly on scaled-up particles, so that they are already adapted to the coarse grain factor to represent the flow behavior accordingly. To further reduce the resulting deviations in the flow behavior of the bulk material the relative particle size distribution of the active material remains the same. The coarse grain factor is set to 100. According to Feng et al.,^[55] such large values are around the upper limit of this method.

To further reduce computation times, a popular method of periodic boundary conditions can be applied. For this purpose, it is necessary to take a closer look at the geometry of the mixer as it is shown in **Figure 2**. The mixing element consists of six similar sections. The blades of the mixing element are alternately mirrored and the individual disks are each mounted on the shaft with an offset of 90°. Thus, a representative element can be extracted from the mixer domain and assumed to be periodic. This assumption implies that boundary effects have a negligible influence on the statistical consideration of stress. As a result, the considered domain is reduced to 1/3 which greatly reduces computational costs.

The calibration of the material parameters for the DEM was carried out by measurements of the static and dynamic angle of repose. Since the relationships between the DEM parameters and the flow behavior of fine powders are very complex, especially when cohesive forces occur, a convolutional neural network was used for this purpose. The video recordings of the flow behavior were converted to binary images using image processing algorithms and fed to the previously trained network. A detailed description of this calibration method will be presented in a future publication. All calibrated DEM parameters are shown in **Table 1**.

The results of the DEM simulations provide boundary conditions for shaping the breakage rate of individual particle size classes. Two quantities are of particular interest. The contact

Table 1. Calibrated DEM parameters of the scaled-up particles.

Parameter	Symbol	Unit	Material	
			Steel	Particle
Density	ρ	kg m^{-3}	7800	1670
Poisson's ratio	ν	–	0.3	0.25
Coefficient of restitution	e	–	0.28	0.21
Coefficient of static friction	μ_{static}	–	0.75	0.83
Coefficient of dynamic friction	μ_{dynamic}	–	0.65	0.68
Surface energy	Γ_{SJKR}	J/m^2	0.78	0.27

frequency \dot{n} and the stress intensity σ . The latter can be represented as both energy and stress, as described in Section 2.3.2. Since both are not homogeneous along the geometry of the mixer, the domain is resolved using a grid that is divided in radial, tangential, and axial directions into 10, 72, and 8 cells, respectively (Figure 2). In each of the 5760 cells, a mass averaged stress tensor is calculated and assigned to the cell. The stress tensor is composed of the normal stresses σ_x , σ_y and σ_z , and the shear stresses τ_{xy} , τ_{xz} and τ_{yz} . One way to make the stress state independent of the coordinate system is to calculate the principal stresses. These form eigenvalues of the stress tensor. The great advantage of this evaluation is that information about the shear stresses is also preserved while at the same time the data size is reduced from six scalars to three. For reasons of simplification, we reduce it further and consider only the mean stress $\bar{\sigma}$ which is the mean of the three principal stresses. As mentioned before, compression and shear dominate in this apparatus. Therefore, it is also possible to use the maximum shear stress τ_{max} instead of $\bar{\sigma}$ to describe the stress with

$$\tau_{\text{max}} = \frac{\sigma_I - \sigma_{III}}{2} \quad (13)$$

However, the performed DEM simulations show that in this case both values are distributed very similarly both quantitatively and spatially.

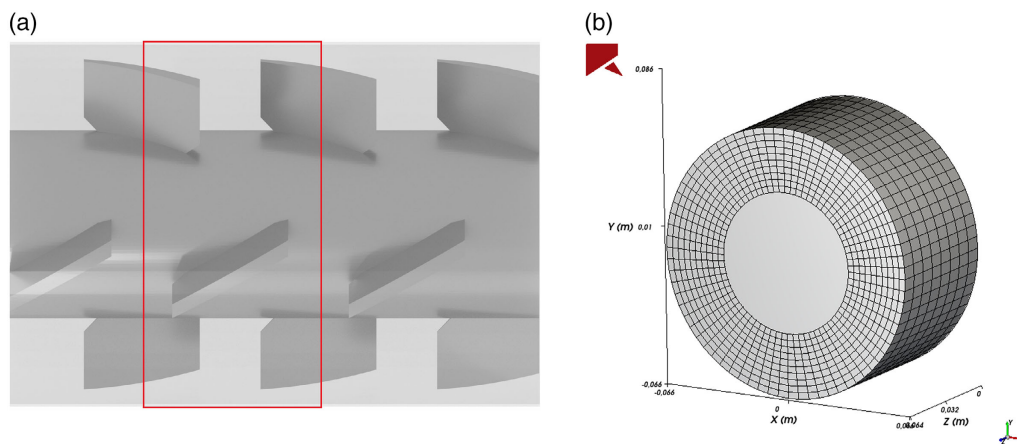


Figure 2. a) A segment of the mixer geometry as a representative element with periodic boundary conditions (red). b) Grid created for Eulerian statistics of the particle interaction data within the periodic element.

2.5. Study Setup

The fracture behavior of the CB agglomerates is described by their fracture strength and the breakage function as described in Section 2.3.2 and depends on the size and nature of the agglomerates. Both power-law and σ_{50} model already include a dependence of the fracture strength on agglomerate size.

The homogeneous breakage function described in Section 2.3.1 can be assumed to be the same for soft and brittle agglomerates. Assigning a separate homogeneous breakage function for soft and brittle agglomerates allows the modeling of different fracture mechanisms due to the nature of the agglomerates. However, an assignment of agglomerates according to existing bond forces is neither experimentally nor simulatively possible. Therefore, the separation between brittle and soft agglomerates is done according to their size. Brittle aggregates form agglomerates with $x < 0.766 \mu\text{m}$ and soft agglomerates with $x \geq 0.766 \mu\text{m}$. This limit is justified only by the shape of the particle size distribution, which as a mass-based distribution shows a characteristic valley at $x \approx 0.766 \mu\text{m}$. As will be seen later, this value is by no means constant, so this remains only a rough estimate. However, this assumption allows a description of the heterogeneous fracture behavior. For this purpose, soft and brittle agglomerates each receive their own homogeneous breakage function. After successful calibration, the best-fit parameters are transferred to tip speeds of 6.25 and 13 m s^{-1} . At this point, the assumption of the process-independent breakage function is to be verified. As already experimentally demonstrated by Wu et al.,^[56] the breakage function often depends on the stress intensity. For this reason, another calibration step is performed for tip speeds 6.25 and 13 m s^{-1} . Based on the previously calibrated parameter set, the breakage functions undergo another calibration process. The fracture strength remains unchanged.

The four studied cases can be summarized as follows.

Case I: Breakage function is homogeneous for the entire particle set, all parameters are optimized.

Case II: Breakage function is split according to the distinction between brittle and soft agglomerates with a homogeneous breakage function for each of the two groups, all parameters are optimized.

Case III: The best-fit parameters for fracture strength and breakage function from Case II are transferred to tip speeds of 6.25 and 13 m s^{-1} , no further parameter optimization.

Case IV: The best-fit parameters for the fracture strength from Case II are transferred to tip speeds of 6.25 and 13 m s^{-1} . The parameters of the breakage functions are again subjected to optimization. Best-fit parameters from Case II are the initial conditions point of the iteration.

2.6. Parameter Calibration

The choice of the parameters for the population balance requires first of all an exact consideration of the physical fracture processes. All parameters can be combined as one vector ξ . The deviation between the measured particle size distribution $f(x, t)$ and the function $\hat{f}_\xi(x, t)$ obtained from the integration of the population balance is the error function $\varepsilon(\xi)$ which is equivalent to a total squared error

$$\varepsilon(\xi) = \|f_{\text{exp}}(x, t) - \hat{f}_\xi(x, t)\|_2^2 \quad (14)$$

The search for the minimum of a function occupies a large and, especially for engineering, an important part of mathematics. Classical methods such as Newton, Gauss–Newton, or Levenberg–Marquardt algorithm, which is a further development of the Gauss–Newton method, require the calculation of the Jacobian matrix, which contains the partial derivatives of the function to be minimized. For functions whose prescription is not known, an elaborate numerical approximation of the partial derivatives is necessary. Furthermore, such methods have a crucial weakness for functions that partly contain shallow valleys. At this point, the convergence speed decreases strongly and a minimum is reached very slowly or not at all. A common example of such behavior is the Rosenbrock function,^[57] which is often used as a benchmark for optimization algorithms. The problem at hand also contains the challenge of the missing expression $\varepsilon(\xi)$ for exact computation of the Jacobian matrix. Furthermore, the optimization of the parameters of the breakage function is not successful with gradient methods due to the many shallow valleys in $\varepsilon(\xi)$. For this reason, a heuristic method is resorted to at this point. In general heuristic methods revolve around obtaining a near-optimal solution within reasonable computational effort while reducing the likelihood of obtaining a bad solution.^[58,59] The method used in this work is the Nelder–Mead algorithm, which is also known as the downhill simplex method.^[60] This method uses a simplex, the simplest volume spanned in a space with n parameters of $n + 1$ points $\xi_0, \xi_1 \dots \xi_{n+1}$. Since each of the points ξ_i in the simplex can be assigned a function value $\varepsilon(\xi_i)$, the points can be sorted according to the function value. By successively reflecting the point with the worst function value, the simplex moves to the local minimum, accumulates around it, and contracts around it by shrinking. While this method is clearly inferior to gradient methods in terms of speed of convergence, it convinces with remarkable robustness. However, the problem of local optima still remains a non-negligible aspect of numerical optimization. A simple way to improve the quality of the results is to perform the optimization with a set of initial conditions $\xi_{0,i}$ with $i = 1..n$. In the presented study, Cases I and II are studied with a randomized set of at least 15 vectors $\xi_{0,i}$. In Case IV $\xi_{0,i}$ is chosen from the best results of Case II.

At least as important as the choice of the optimization algorithm is the preconditioning of the parameter vector ξ . This is implemented in two steps in this work. First, the preconditioning changes the scale of the parameters. This is especially important for parameters whose influence is nonlinear or suspected to be nonlinear. The calculation of the individual parameters is shown in Equation (15a–e). The logarithmic consideration of the parameters improves the resolution for $q \approx 1$ and smaller values of v . The values for σ_{50} and σ_{end} are also logarithmically scaled, since the values of fracture strength cover large ranges of values. The second step of preconditioning normalizes the parameter vector $\hat{\xi}$. This is the simplest type of preconditioning that improves numerical accuracy.

$$\hat{q} = \log_{10} q \quad (15a)$$

$$\hat{v} = \log_2 v \quad (15b)$$

$$\hat{\sigma}_0 = \log_{10} \sigma_0 \quad (15c)$$

$$\hat{\sigma}_{\text{end}} = \log_{10} \sigma_{\text{end}} \quad (15d)$$

$$\varepsilon(\xi) = \frac{\sigma_p}{\xi_0} \quad (15e)$$

2.7. Measurement of Particle Size Distribution

Measuring the particle size distribution of CB is a huge challenge. To measure the particle size distribution, several samples, each with 0.5 g, are taken from the dry mixture. Then, these are mixed manually with 0.5 g stabilizer for 2 min. As the next step, the samples are suspended each in 12 g *N*-methyl-2-pyrrolidone (NMP), a common organic solvent used in Li-ion battery manufacturing, by hand for 2 min. Since NCM is also added during the mixing process, it must be removed from the sample after the mixing process. For this purpose, the prepared suspension is treated in a centrifuge at 500 rpm for 5 min. During this process, a separation between CB and NCM takes place due to the difference in size and density. The particle size distribution of the CB in the suspension is then measured by light scattering. A detailed description of this method and its evaluation can be found in the publication by Dreger et al.^[61]

At this point, the influence of the measurement procedure on the resulting size distributions is to be noted. Manual mixing with the stabilizer, suspension in NMP, and centrifugation can lead to further comminution and/or reagglomeration of the CB agglomerates. Furthermore, measurement methods using light scattering usually provide equivalent diameters based on spherical particles. Especially in the case of fractal structures of the CB, these can deviate significantly from the actual size. This error influences the results of the simulations due to the conversion of the agglomerate sizes to volumes x to calculate the population balance (Section 2.1). Nevertheless, these influences can hardly be prevented, since alternative measurement methods either involve a significantly higher effort or comparable assumptions and effects.

The investigated blends are part of an experimental study. The measurements of NCM and CB (3 wt%) premixed under low energy input are taken as the initial value. The target

distributions are obtained from the samples mixed at a tip speed of 6.25, 9.5, and 13 m s⁻¹ for 2 min. In each test, 300 g of powder is added to the mixer. Each particle size distribution is obtained from the average of at least six samples.

3. Results and Discussion

3.1. Collision Data from DEM Simulations

The density distributions of the mean stress are shown in **Figure 3** (left). Both the maximum stresses and the x_{50} value shift to larger stresses as the tip speed of the mixing tool increases. **Figure 3** (right) shows a spatial distribution of the mean principal stress in the mixer at 9.5 m s⁻¹. As expected, the stress is concentrated in the areas in front of the mixing blades, where the particles accumulate. Here, the bulk is compressed and the stress reaches its peak at the contact points with the geometry.

The particle contact frequency is also averaged within each cell. Since the total number of stress events $N_{p,i}$ in cell i also depends on the number of particles in the system, the average is normalized by the number of particles in the system. This partially compensates for the error generated by the coarse-grain approach. A similar approach was already applied in the study of wet grinding.^[62] **Figure 4** (left) shows the specific contact frequencies for the DEM simulation at different mixing speeds. Here, the values are assigned to the corresponding mean stress in the cells of the applied grid. **Figure 4** (right) shows the spatial distribution of the specific contact frequencies.

The total number of stress events for a stress intensity is assumed to be proportional to the integral of the specific frequency over all stresses in the mixer exceeding the critical breaking stress σ_{crit} and is corrected by a constant scalar λ

$$\dot{n}(\sigma_{\text{crit}}) = \lambda \int_{\sigma_{\text{crit}}}^{\sigma_{\text{max}}} \dot{n}(\sigma) d\sigma \quad (16)$$

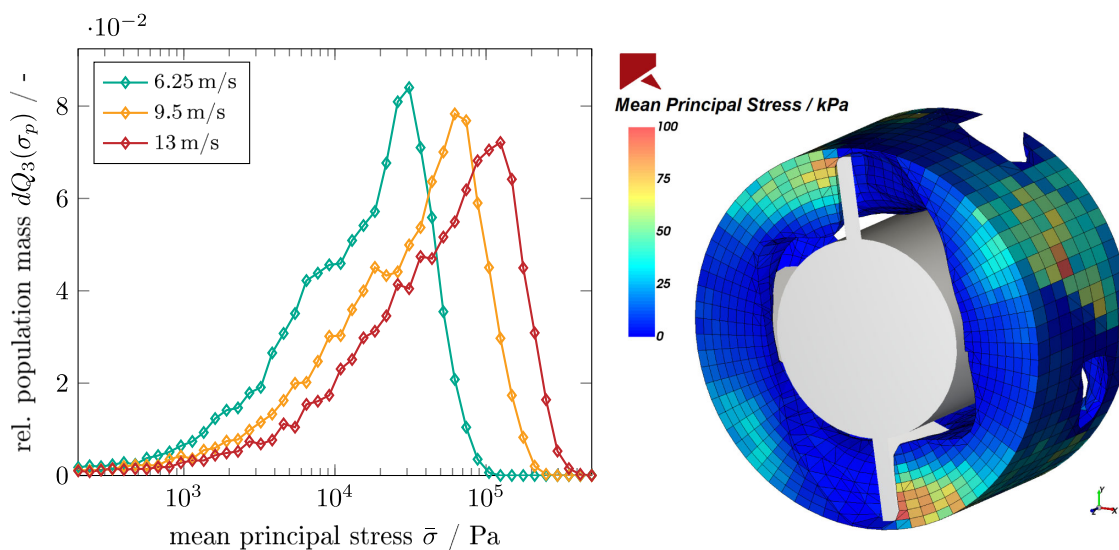


Figure 3. Left: Quantitative distributions of the mean stress at different tip speeds. Right: Spatial distribution of the mean stress at $v_{\text{tip}} = 9.5 \text{ m s}^{-1}$.

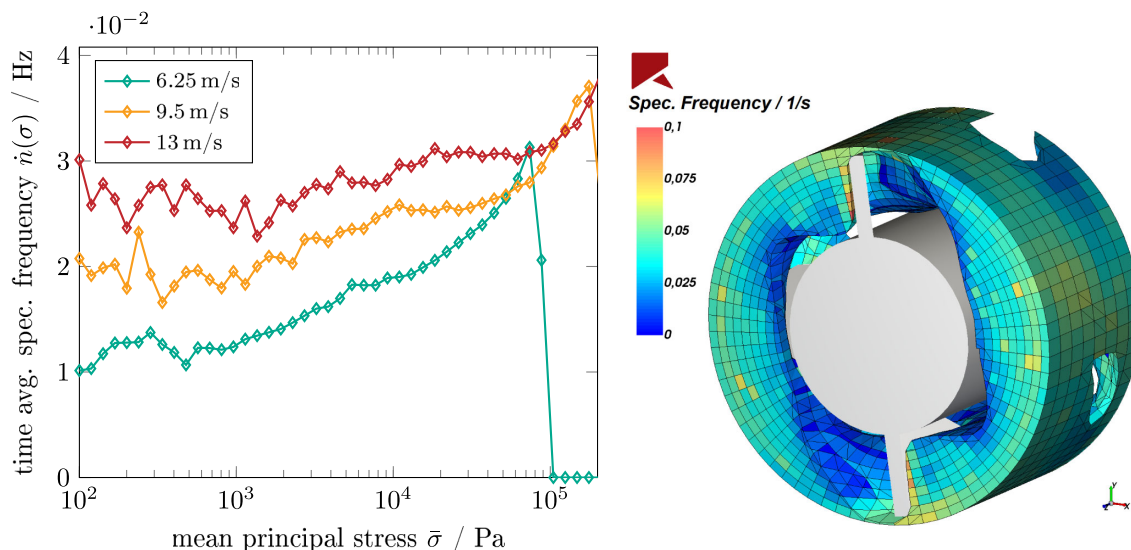


Figure 4. Left: Time average specific frequency for different values of the mean stress at different tip speeds. Right: Spatial distribution of the average specific frequency at $v_{tip} = 9.5 \text{ m s}^{-1}$.

3.2. Case I

Figure 5 shows the mass-based population distribution after successful optimization of the parameters for the exponential model of the critical fracture stress and a homogeneous breakage function in comparison with the experimentally determined values.

The disadvantage of the homogeneous approach is clearly evident. The bimodal nature of the particle size distribution is almost completely lost. On closer inspection, however, it is noticeable that the resulting distribution can be described as a sum of three broad monomodal distributions. This effect may be a consequence of the modeling.

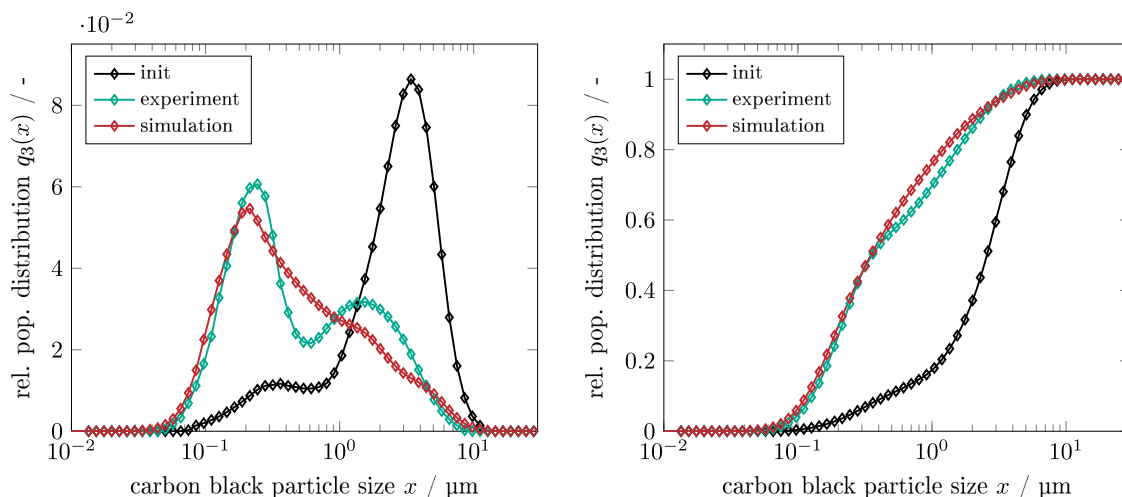


Figure 5. Simulation results for homogeneous breakage are compared to experimental measurements and initial state. Left: Mass-based carbon black (CB) particle size population distribution. Right: Cumulative mass-based CB particle size distribution.

3.3. Case II

The results of the simulations with a heterogeneous kernel show a very similar course for both applied models of fracture strength (**Figure 6**). The division of the entire distribution into three monomodal distributions, already observed in the homogeneous approach, is more pronounced here. This means that the distributions are now narrower and the curve better captures the valley between soft and brittle agglomerates.

Furthermore, there is little difference between the two breakage models. The breakage rates for the best-fit parameters of both fracture models are shown in **Figure 7**. With particularly high fracture strengths, both models prevent the comminution of small

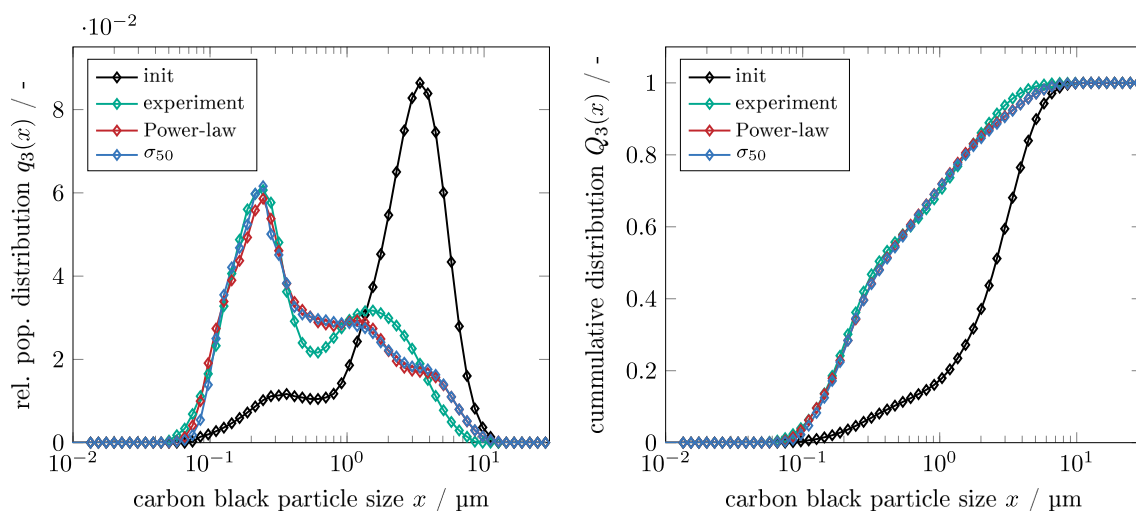


Figure 6. Simulation results for heterogeneous breakage with power-law and σ_{50} fracture strength models are compared to experimental measurements and initial state. Left: Mass-based CB particle size population distribution. Right: Cumulative mass-based CB particle size distribution.

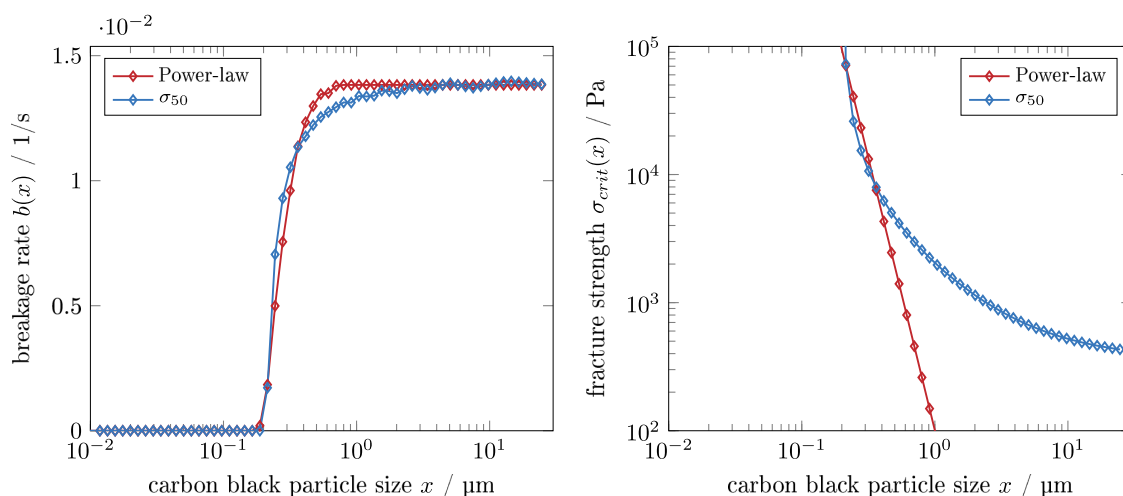


Figure 7. Breakage parameters after successful calibration at $\nu_{tip} = 9.5 \text{ m s}^{-1}$ for power-law and σ_{50} models. Left: Breakage rate. Right: Fracture strength.

agglomerates. The increase in the breakage rate is influenced by the slope of the fracture strength. As a result, the course of the breakage rate of the power-law model is slightly steeper. However, both functions end in a constant value for large agglomerates. Another characteristic of the breakage rate is the limit value of $x_{lim} \approx 0.2 \mu\text{m}$. With $b(x < x_{lim}) = 0$, the breakage rate reproduces a limited breakage. While the σ_{50} model imposes this limit with $x_p = 0.199 \mu\text{m}$, the power-law model implements this by a very steep gradient. This behavior is consistent with the observations of Mayer et al.^[63] Here, wet dispersion of CB in a planetary mixer also showed a limit at $0.2 \mu\text{m}$. The same was confirmed with micro-scale DEM simulation.^[64]

The values of the optimized parameters of the breakage function are shown in Table 2. The breakage functions for both fracture strength models are shown in Figure 8. The breakage function for brittle agglomerates (Figure 8 left) is a narrow distribution with few fragments for both fracture models. The

Table 2. Optimized breakage function parameters for soft and brittle agglomerates at $\nu_{tip} = 9.5 \text{ m s}^{-1}$.

	Power-law			σ_{50}		
	q	ν	z_{50}	q	ν	z_{50}
Brittle agglomerates	3.8	27.6	3.08×10^{-2}	3.7	18.5	4.59×10^{-2}
Soft agglomerates	2.1	46.8	1.68×10^{-2}	0.2	158.2	9.86×10^{-4}

values for the fracture type q and fragment number ν are also very close. Only a higher fragment number in the power-law model shifts the z_{50} value to the left. The similarity is most likely due to the fact that the fracture strength in the range $x < 0.766 \mu\text{m}$ has a very similar course for both models.

The breakage functions of the soft agglomerates (Figure 8 right), on the other hand, look different for the two models.

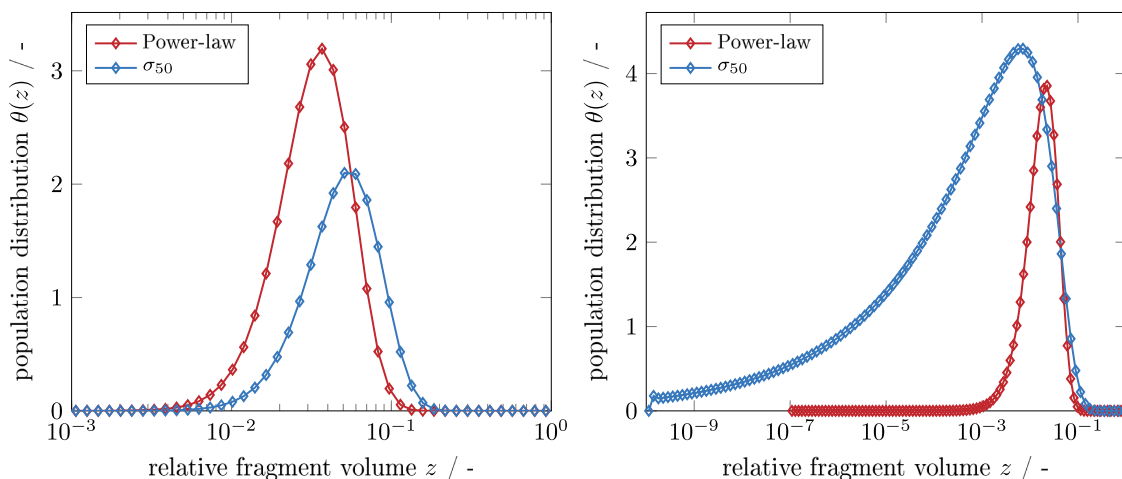


Figure 8. Breakage functions after successful calibration at $v_{tip} = 9.5 \text{ m s}^{-1}$ for power-law and σ_{50} models. Left: Brittle agglomerates. Right: Soft agglomerates.

While the breakage function of the power-law model converges to a narrow distribution with $q > 1$ and $z_{50} = 1.68 \times 10^{-2}$, the breakage function of the σ_{50} model forms an asymmetric function corresponding to erosion with $q < 1$. Since σ_{50} model assumes much higher values for fracture strength of soft agglomerates compared to the power-law model. Thus, the breakage rate in this region is lower than in the power-law model. Since experimental data dictates a certain extent of breakage within the specified time, the parameters of the breakage function compensate for this influence with a higher amount of smaller fragments.

3.4. Case III

Assuming that both the breakage function and the fracture strength are process independent, the best-fit parameters are applied to other tip speeds. The values for the error $\epsilon(\xi_{best})$ are shown in **Figure 9**. The error values for 6.25 and 13 m s^{-1} are

an order of magnitude larger than for the simulation with the original tip speed of 9.5 m s^{-1} .

The agreement of the simulation results with the experimentally determined values is good for a tip speed of 13 m s^{-1} . The characteristic valley for soft agglomerates is smoothed similar to case I. However, the dominant peak of the brittle agglomerates is reproduced with very good accuracy. Nevertheless, the dominant peak of brittle agglomerates is simulated with a very good accuracy. In contrast, the simulation results for $v_{tip} = 6.25 \text{ m s}^{-1}$ deviate significantly from the measured values with increasing agglomerate size x .

3.5. Case IV

The limitation of the process-independent breakage function is lifted. The best-fit parameters for the fracture strength are retained, while the parameters are optimized with ξ_{best} as the starting point. The errors can be seen in **Figure 9** (right). The

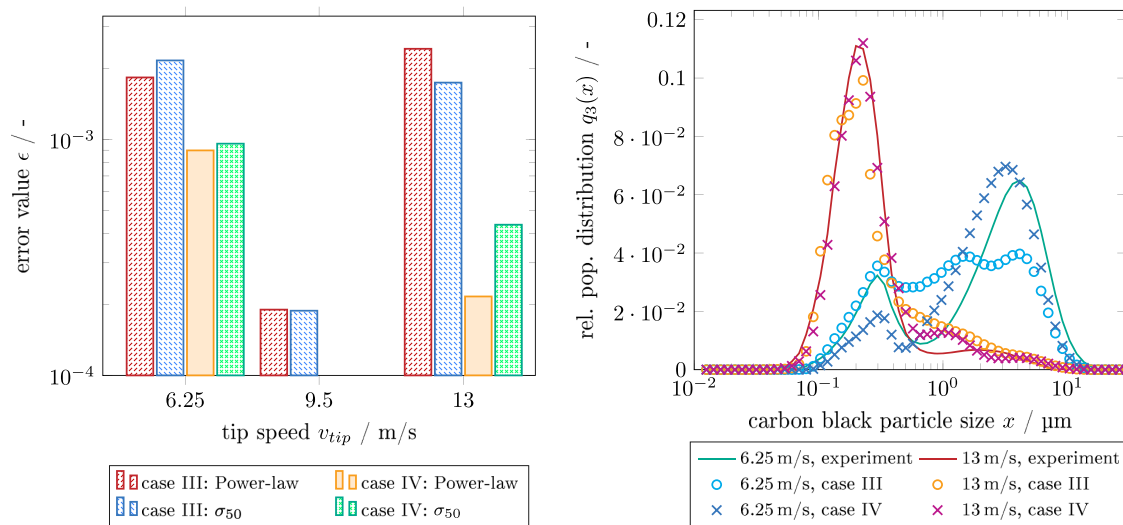


Figure 9. Left: Total squared errors for Cases III and IV at different tip speeds. Right: population size distributions at different tip speeds of Cases II and IV compared to experimental results.

Table 3. Optimized breakage function parameters for soft and brittle agglomerates at all tip speeds.

	– $v_{tip}/m\ s^{-1}$	power-law			σ_{50}		
		q	v	z_{50}	q	v	z_{50}
Brittle agglomerates	6.25	13.0	15.0	6.0×10^{-2}	45.6	17.2	5.4×10^{-2}
	9.5	3.8	27.6	3.1×10^{-2}	3.7	18.5	4.6×10^{-2}
	13	1.3	17.2	5.8×10^{-2}	0.9	13.1	5.0×10^{-2}
Soft agglomerates	6.25	1.6	4.0	2.1×10^{-1}	1.6	4.0	2.1×10^{-1}
	9.5	2.1	46.8	1.7×10^{-2}	0.2	158.2	9.8×10^{-4}
	13	6.8	4.0	1.1×10^{-2}	145.8	60.0	1.5×10^{-2}

parameters for all breakage functions are shown in Table 3. For the sigma model, the z_{50} remains constant at $\approx 5 \times 10^{-2}$ while the width of the distribution decreases with increasing tip speed. For $13\ m\ s^{-1}$, the break function takes the form of a random fragment size distribution with $q \approx 1$. Similar to Case II, this has less of a physical background, but is due to simplified modeling.

The width of the breakage function for brittle agglomerates increases for the power law model with increasing tip speed. For the sigma model, the z_{50} remains constant at $\approx 5 \times 10^{-2}$ while the width of the distribution decreases with increasing tip speed. For $13\ m\ s^{-1}$, the breakage function takes the form of a random fragment size distribution with $q \approx 1$.

For $6.25\ m\ s^{-1}$, the soft agglomerates breakage functions for power-law and sigma-model are almost identical and represent a random fragment size distribution with very few fragments. For $13\ m\ s^{-1}$, the breakage function for the sigma model approaches fragmentation into equal-sized fragments.

Due to the simplified modeling, the interpretation of the results is very difficult. As previously described the parameter values are due to the specification of the extent of breakage. Furthermore, the parameters had to be limited to physical values. As described in Section 2.3.1, at least two fragments must be created in each breakage event. For this reason, parameters with $v < 2$ are sorted out, even if the simulation results showed very small errors.

Neither the σ_{50} nor the power-law model did show a significant advantage in the presented setup. However, the main focus of the calibration appears to be the smaller particle sizes. This is evident in a better accuracy in the prediction of the size distribution in Figure 9 (right) and the prioritized enforcement of the breakage limit. Also, the calibrated parameters for the breakage function of soft agglomerates show a distinctive pattern both for σ_{50} and the power-law models. Here the number of fragments at tip speed of $9.5\ m\ s^{-1}$ is significantly higher than that of other regarded tip speeds. Even more interesting is the fact that with $q = 0.2$ the breakage function suggests erosion breakage. One possible explanation is the absence of agglomeration in the model. With this restriction, it is the only way to produce fine particle classes while simultaneously slowing down the mass reduction of large particle classes. On lower tip speeds this is not necessary since the overall breakage rate is lower due to lower stress intensity and frequency (see Figure 3 and 4). At higher tip speeds, the effect of reagglomeration is less dominant due to high-stress intensity and frequency and the low particle strength of soft agglomerates. Another crucial aspect is the validity of the linearity

of the breakage. Bilgili and Scarlet provide a very sobering insight into the reality of particle breakage.^[65] They describe three different types of non-linearity which result in a time-variant breakage rate. Especially the last two types can explain the residual errors in particle size prediction. Both types are caused by the increase in volume of fine particle classes. These create damping layers within the bulk and reduce the applied stress.^[22,66] Similar effects were also observed during the calibration of the DEM parameters. Here the flow behavior of the bulk showed a dependence on the extent of breakage of CB (Figure A1).

4. Conclusion and Outlook

Modeling CB comminution during dry mixing is a task with many challenges. Basic modeling using population balances provides a good and proven method. Both material and process properties need to be defined, measured, or modeled to describe the birth and death terms. The process properties can be determined by means of DEM simulations. By considering the contact frequency and the resulting stress within the bulk, the influence of the process properties can be implemented in the population balance. The material properties like breakage function and fracture strength can be modeled with simple models with a physical background. None of the used models show an advantage in this respect. The DEM simulations require many simplifying approaches, but provide a good qualitative representation of the impact frequencies and intensities. The breakage frequency, which is a combination of the specific contact frequency and the required fracture stress, suggests a limited breakage. The values of the breakage limit are comparable to those found in the literature.

The interpretation of the breakage functions, in contrast, is difficult. The optimized parameters are strongly influenced by the calibration of experimental data. The assumption of homogeneous breakage behavior shows very good agreement with the measured values with respect to x_{50} , but reduces the results to a quasi-monomodal distribution. With the division of the agglomerates into brittle and soft agglomerates based on a size limit, the MOC unfolds its advantage and reproduces the measured values much better. The transfer of the parameters to other process settings results in a good representation of the agglomerate size distribution without recalibration of the breakage function only at high tip speeds. However, for lower speeds, recalibration of the breakage function provides a significant improvement in the simulation.

The focus of further investigations is on the improvement of the previously made assumptions and simplifications. Thus, the modeling of the reagglomeration is mandatory if a binding agent is added to the mixtures. However, reagglomeration can also be a non-negligible aspect when processing without binders. Furthermore, a resolved view of the mixer domain can improve the simulation results. However, the locally resolved population balance equation using the MOC introduces significantly higher computational costs. Recently, Peterson et al.^[67] presented a new framework for numerically solving the population balance equations, which they applied to locally resolved computation within flow simulations. This approach together with the work of Vikhansky et al.^[68] provides promising alternatives to MOC without completely sacrificing the advantages of resolved representation of the size distributions.

Appendix

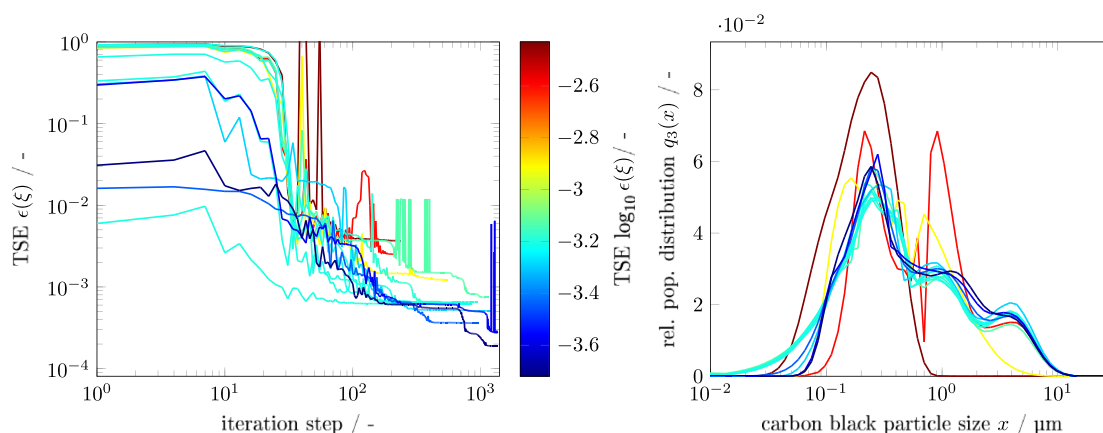


Figure A1. Left: Total squared error of the optimization with varied initial conditions. Right: Terminal population distributions of CB for the optimization with varied initial conditions.

Acknowledgements

The Federal Ministry of Education and Research (BMBF) and Project Management Jülich (Ptj) throughout the project O3XP0239 (MultiEx) are highly acknowledged. Furthermore, the authors thank all scientists within the ProZell research cluster for rewarding exchanges. Special thanks to CADFEM for providing the ROCKY DEM software license and in particular to Dr. Jan-Philipp Fürstenau for the numerous discussions regarding the DEM simulation setup.

Open Access funding enabled and organized by Projekt DEAL.

Conflict of Interest

The authors declare no conflict of interest.

Data Availability Statement

Research data are not shared.

Keywords

carbon black, discrete element method, dry mixing, Li-ion batteries, modeling, population balance equation, simulations

Received: July 31, 2022

Revised: September 24, 2022

Published online:

- [1] I. Tsiropoulos, D. Tarvydas, N. Lebedeva, in *Li-Ion Batteries For Mobility and Stationary Storage Applications*, Springer, Berlin, Germany **2018**.
- [2] N. H. Kwon, H. Yin, P. Brodard, C. Sugnaux, K. M. Fromm, *Electrochim. Acta* **2014**, *134*, 215.
- [3] Y. H. Chen, C. W. Wang, X. Zhang, A. M. Sastry, *J. Power Sources* **2010**, *195*, 2851.

- [4] B. Vijayaraghavan, D. R. Ely, Y.-M. Chiang, R. Garcia-Garcia, R. E. Garcia, *J. Electrochem. Soc.* **2012**, *159*, A548.
- [5] G.-W. Lee, J. H. Ryu, W. Han, K. H. Ahn, S. M. Oh, *J. Power Sources* **2010**, *195*, 6049.
- [6] H. Nakajima, T. Kitahara, Y. Higashinaka, Y. Nagata, *ECS Trans.* **2015**, *64*, 87.
- [7] V. Wenzel, H. Nirschl, D. Nötzel, *Energy Technol.* **2015**, *3*, 692.
- [8] K. Miyasaka, K. Watanabe, E. Jojima, H. Aida, M. Sumita, K. Ishikawa, *J. Mater. Sci.* **1982**, *17*, 1610.
- [9] S. P. Rwei, F. H. Ku, K. C. Cheng, *Colloid Polym. Sci.* **2002**, *280*, 1110.
- [10] R. Dominko, M. Gaberšček, J. Drogenik, M. Bele, J. Jamnik, *Electrochim. Acta* **2003**, *48*, 3709.
- [11] J. J. Richards, J. B. Hipp, J. K. Riley, N. J. Wagner, P. D. Butler, *Langmuir* **2017**, *33*, 12260.
- [12] V. Wenzel, R. S. Moeller, H. Nirschl, *Energy Technol.* **2014**, *2*, 176.
- [13] W. Bauer, D. Nötzel, V. Wenzel, H. Nirschl, *J. Power Sources* **2015**, *288*, 359.
- [14] D. Ramkrishna, in *Population Balances: Theory and Applications to Particulate Systems in Engineering*, Academic, Amsterdam **2000**.
- [15] M. Hsia, L. L. Tavlarides, *Chem. Eng. J.* **1983**, *26*, 189.
- [16] J. A. Gantt, E. P. Gatzke, *Powder Technol.* **2005**, *156*, 195.
- [17] L. Silva, R. Damian, P. Lage, *Comput. Chem. Eng.* **2008**, *32*, 2933.
- [18] A. Mesbah, H. J. Kramer, A. E. Huesman, P. M. V. den Hof, *Chem. Eng. Sci.* **2009**, *64*, 4262.
- [19] Y. Liao, R. Oertel, S. Kriebitzsch, F. Schlegel, D. Lucas, *Int. J. Numer. Methods Fluids* **2018**, *87*, 202.
- [20] M. Singh, K. Vuik, G. Kaur, H.-J. Bart, *Powder Technol.* **2019**, *342*, 972.
- [21] M. Singh, A. Kumar, S. Shirazian, V. Ranade, G. Walker, *Pharmaceutics* **2020**, *12*, 1152.
- [22] D. Fuerstenau, P. Kapur, B. Velamakanni, *Int. J. Miner. Process.* **1990**, *28*, 81.
- [23] P. Toneva, W. Peukert, *Particle Breakage*, Elsevier, Amsterdam **2007**, pp. 873–911.
- [24] J. Kano, F. Saito, *Powder Technol.* **1998**, *98*, 166.
- [25] J. Kano, H. Mio, F. Saito, M. Tanjo, *J. Chem. Eng. Jpn.* **1999**, *32*, 747.
- [26] J. Kano, H. Mio, F. Saito, *AIChE J.* **2000**, *46*, 1694.
- [27] H. Mori, H. Mio, J. Kano, F. Saito, *Powder Technol.* **2004**, *143–144*, 230.
- [28] A. Datta, R. K. Rajamani, *Int. J. Miner. Process.* **2002**, *64*, 181.

- [29] A. Spettl, M. Dosta, S. Antonyuk, S. Heinrich, V. Schmidt, *Adv. Powder Technol.* **2015**, 26, 1021.
- [30] H. Lee, K. Kim, H. Lee, *Adv. Powder Technol.* **2019**, 30, 2517.
- [31] E. W. Montroll, R. Simha, *J. Chem. Phys.* **1940**, 8, 721.
- [32] M. Kostoglou, *Particle Breakage*, Elsevier, Amsterdam **2007**, pp. 793–835.
- [33] J. Kumar, J. Saha, E. Tsotsas, *SIAM J. Numer. Anal.* **2015**, 53, 1672.
- [34] M. Kostoglou, S. Dovas, A. Karabelas, *Chem. Eng. Sci.* **1997**, 52, 1285.
- [35] R. Vigil, R. M. Ziff, *J. Colloid Interface Sci.* **1989**, 133, 257.
- [36] P. J. Hill, K. M. Ng, *AIChE J.* **1995**, 41, 1204.
- [37] L. Austin, K. Shoji, V. Bhatia, V. Jindal, K. Savage, R. Klimpel, *Industr. Eng. Chem. Process Des. Dev.* **1976**, 15, 187.
- [38] B. J. McCoy, M. Wang, *Chem. Eng. Sci.* **1994**, 49, 3773.
- [39] R. Diemer, J. Olson, *Chem. Eng. Sci.* **2002**, 57, 4187.
- [40] J. Winkler, in *Dispergieren Von Pigmenten Und Füllstoffen*, Vincentz Network, Hanover **2014**.
- [41] L. M. Tavares, in *Particle Breakage*, Elsevier, Amsterdam **2007**, pp. 3–68.
- [42] S. Yashima, Y. Kanda, S. Sano, *Powder Technol.* **1987**, 51, 277.
- [43] P. A. Cundall, *Ph. D. Thesis*, University of London, **1971**.
- [44] H. Hertz, *J. Reine Angew. Math.* **1882**, 92, 156.
- [45] R. D. Mindlin, H. Deresiewicz, *J. Appl. Mech.* **1953**, 20, 327.
- [46] K. L. Johnson, K. Kendall, A. D. Roberts, *Proc. Roy. Soc. Lond. A. Math. Phys. Sci.* **1971**, 324, 301.
- [47] G. Nichols, S. Byard, M. J. Bloxham, J. Botterill, N. J. Dawson, A. Dennis, V. Diart, N. C. North, J. D. Sherwood, *J. Pharm. Sci.* **2002**, 91, 2103.
- [48] J.-B. Donnet, A. Voet, in *Carbon Black: Physics, Chemistry and Elastomer Reinforcement*, Dekker, New York **1976**.
- [49] S.-P. Rwei, S. W. Horwatt, I. Manas-Zloczower, D. L. Feke, *Int. Polym. Process.* **1991**, 6, 98.
- [50] S. P. Rwei, I. Manas-Zloczower, D. L. Feke, *Polym. Eng. Sci.* **1991**, 31, 558.
- [51] S.-P. Rwei, I. Manas-Zloczower, D. L. Feke, *Polym. Eng. Sci.* **1992**, 32, 130.
- [52] N. G. Özcan Taskin, G. Padron, A. Voelkel, *Chem. Eng. Res. Des.* **2009**, 87, 468.
- [53] M. Moseler, C. Bierwisch, T. Kraft, H. Riedel, **2009**.
- [54] C. Bierwisch, T. Kraft, H. Riedel, M. Moseler, *J. Mech. Phys. Solids* **2009**, 57, 10.
- [55] Y. T. Feng, D. R. J. Owen, *Comput. Part. Mech.* **2014**, 1, 159.
- [56] S. Wu, K. Chau, T. Yu, *Powder Technol.* **2004**, 143–144, 41.
- [57] H. H. Rosenbrock, *Comput. J.* **1960**, 3, 175.
- [58] S. H. Zanakis, J. R. Evans, *Interfaces* **1981**, 11, 84.
- [59] R. Mart, G. Reinelt, in *Exact and Heuristic Methods in Combinatorial Optimization*, Springer, Berlin Heidelberg **2022**, pp. 27–57.
- [60] J. A. Nelder, R. Mead, *Comput. J.* **1965**, 7, 308.
- [61] H. Dreger, M. Huelsebrock, L. Froboese, A. Kwade, *Ind. Eng. Chem. Res.* **2017**, 56, 2466.
- [62] A. Kwade, J. Schwedes, in *Particle Breakage*, Elsevier, Amsterdam **2007**, pp. 251–382.
- [63] J. K. Mayer, L. Almar, E. Asylbekov, W. Haselrieder, A. Kwade, A. Weber, H. Nirschl, *Energy Technol.* **2019**, 201900161.
- [64] E. Asylbekov, R. Trunk, M. J. Krause, H. Nirschl, *Energy Technol.* **2021**, 9, 2000850.
- [65] E. Bilgili, B. Scarlett, *Powder Technol.* **2005**, 153, 59.
- [66] L. Austin, P. Bagga, *Powder Technol.* **1981**, 28, 83.
- [67] J. D. Peterson, I. Bagkeris, V. Michael, *Chem. Eng. Sci.* **2022**, 259, 117781.
- [68] A. Vikhansky, A. Splawski, *Can. J. Chem. Eng.* **2015**, 93, 1327.